IEEE Access
Multidisciplinary ⋮ Rapid Review ⋮ Open Access Journal

Received August 19, 2021, accepted August 30, 2021, date of publication September 3, 2021, date of current version September 14, 2021.

Digital Object Identifier 10.1109/ACCESS.2021.3110207

Design of Robust Fault-Tolerant Control for Target Tracking System With Input Delay and Sensor Fault

THINH HUYNH[1,2] AND YOUNG-BOK KIM[1], (Senior Member, IEEE)
[1]Department of Smart Robot Convergence and Application Engineering, Pukyong National University, Busan 48513, South Korea
[2]Department of Chassis and Body, Ho Chi Minh City University of Technology and Education, Ho Chi Minh City 700000, Vietnam

Corresponding author: Young-Bok Kim (kpjiwoo@pknu.ac.kr)

This work was supported by the National Research Foundation (NRF), South Korea, under Project BK21 FOUR (Smart Robot Convergence and Application Education Research Center).

ABSTRACT This paper presents a robust fault-tolerant control scheme that provides reliable tracking and effective disturbance rejection for a low-cost tracking system. As the controlled apparatus, a 2-axis gimbaled mechanism is involved in a networked control system, and an unreliable sensor brings sensor drift into the system. Besides, external disturbances heavily affect the system in practical applications. Representation of the faulty gimbal system with its constraints and disturbances is firstly introduced. Then, the design of the fault-tolerant controller is detailed, which consists of two components: (1) an unknown input observer that estimates the fault and effect of disturbances and network delay simultaneously, and (2) a robust control law, using the observer estimations, designed based on the combination of the super-twisting algorithm, backstepping procedure, and integral sliding mode control technique. Subsequently, simulations and experiments are conducted, in which the performance of the proposed control system is compared to those from the previous studies. The results show the superiority and reliability of the proposed control system.

INDEX TERMS Fault tolerant control, target tracking system, time-varying delay, unknown input observer, sensor drift, integral sliding mode control.

I. INTRODUCTION

For tracking a target of interest from a mobile platform, gimbaled mechanisms are usually used to control the line-of-sight (LOS) of the tracking device [1]–[6]. These mechanisms are electromechanical structures that consist of several orthogonal rotating channels. The number of channels is two or more depending on the degrees of freedom that need controlling. For instance, a two-axis gimbal can control the tilt and pan motion of the device carried by the inner channel. The tracking device, such as camera modules, radars, or laser sensors, is carried by the inner channel of the gimbal. However, in some configurations, the device is fixed to the vehicle carrying the gimbal while a mirror or other optical elements are mounted on the inner channel to reflect the sensor's LOS [5], [7]. In both configurations, the gimbal serves as a stabilizing platform that isolates the LOS from the external motions and disturbances, and at the same time, it steers the LOS to track accurately the desired target. The gimbal itself is a simple structure, but its dynamics are complex with nonlinear factors, coupling, and external disturbances, especially the vehicle motion [5]–[9]. Therefore, popular control schemes for the system are H∞ [10], [11], sliding mode [12]–[14], or active disturbance rejection [15], thanks to their robustness when facing disturbances.

The LOS orientation corresponds to the posture of the device at the inner channel, which is measured by an inertial measurement unit (IMU) or an attitude heading reference system (AHRS). Both consist of three individual sensors that measure accelerations, angular rates, and geomagnetism of the attached object in the inertial space. The angular positions are firstly integrated from the corresponding angular rates measured by the gyroscopes. Imperfect hardware and non-ideal operating conditions of the sensor, such as incorrect calibration and long sampling time, make the integrations cannot be trusted. Therefore, the roll and pitch angles are

The associate editor coordinating the review of this manuscript and approving it for publication was Ton Duc Do.

corrected with the direction of the gravitational acceleration measured by the accelerometer. On the other hand, the yaw angle is corrected by using the geomagnetism measured by the magnetometer. However, the signal from the magnetometer may be small enough that it is insufficient to set the angle. Then, the yaw drift phenomenon appears [16]–[19] and leads to incorrect measurements of the corresponding pan rotation of the inner gimbal. This is one of the most frequent faults occurring in a gimbal system. Existing methods compensating for this gyro drift try to correct the sensor measurement, either by calibrating the gyroscope [19], filter measurement error [16], or correcting the orientation measurement with additional sensors [18]. However, they often struggle to preserve their efficiency, especially in harsh operating conditions. Moreover, control methods for the system having this sensor fault are seldom tackled.

Automated systems are vulnerable to faults, which might lead to instability or failure of performing required tasks. Generally, faulty conditions could come from either actuator, sensor, connection, or the system itself. Fault-tolerant control (FTC) systems are capable of maintaining the overall system stability and acceptable performance in the event of faults and failures. Passive FTCs rely on robust control techniques, such as H∞ and sliding mode, to compensate for unwanted effects of the faults on the system without any knowledge of the faults. On the contrary, active FTCs rely on information obtained by fault detection and isolation (FDI) schemes to adjust their control laws accordingly. Designing of FTCs and FDIs has been receiving allotted attention in many engineering applications. Especially, with the development of complex automated systems and smart factories, this continues to be an active area of research in the control community. Many aspects of the active FTC have been covered in the overview studies [20]–[23]. For designing the FDI, full-state observers [24], [25], unknown input observers [26], [27], time-delay estimation [28], and numerous approaches have been proposed. The main difficulty of designing FDIs remains at decoupling the fault from other unknown factors, such as disturbances, perturbed parameters, and time delay. For the FTC law, the issue is to incorporate the fault information in the control law such that the influence of the faults is compensated while the system stability is still preserved. Adaptation [26], switching [29], reconfiguration [24], and robust control laws [25] are popular techniques that have been adopted and implemented.

On the other hand, the collaboration of low-cost devices and advanced control algorithms is always desirable to achieve both economical and technical objectives. Unfortunately, low-cost hardware usually comes with limited performance and reliability. For instance, the use of networked control systems is currently attractive due to their simplicity and cost-effectiveness. However, long sampling time and inevitable communication delay restrict the achievable performance of the systems [30], [31]. Additionally, the probability that a fault occurs is obviously higher in a system equipped with unreliable components. Hence, control problems become more difficult with low-cost systems. Especially, few fault-tolerant control techniques are successfully implemented in these systems. Therefore, there is a need for advanced controls that overcome the limitations of the system, compensate for the faults occurring, and ensure the effectiveness and robustness of the system.

In this paper, we propose a robust fault-tolerant controller for a tracking system with the abovementioned drawback. This paper extends the author's preliminary work in [32], which was accepted to be presented. In detail, the system operation is highly influenced by disturbances from the carrying vehicle, nonlinearities of the gimbaled mechanism, time-varying delay of the networked control configuration, and yaw drift fault of the AHRS. These factors are firstly demonstrated in the mathematical representation of the system. Secondly, an unknown input observer (UIO) is proposed to identify the fault and estimate the effects of delays and disturbances. Then, the fault-tolerant control scheme is derived from a combination of the backstepping technique, super-twisting algorithm, and integral sliding mode strategy. Comparative simulations and experiments are conducted to validate the efficiency of the proposed control system. Accordingly, the contributions of this paper can be listed as follows:

- The problem of controlling a gimbal system in the presence of delayed input and sensor drift is firstly tackled.
- The novel FTC is proposed for a system affected by input delay, disturbances, and sensor fault simultaneously.
- The design of the UIO for nonlinear systems affected by time delay, sensor fault, and disturbances, that is able to estimate simultaneously the system state, fault, and the effect of the disturbances and time delay.
- A combination of the backstepping technique, integral sliding mode control, and the super-twisting algorithm is proposed. Additionally, the boundedness of the sliding variable with the chattering-reduced super-twisting controller is given for the first time.

The remainder of the paper is distributed in 5 sections. Section 2 describes the mathematical model of the faulty target tracking system. The estimation of fault and disturbances is achieved with the UIO designed in Section 3. Section 4 presents the design process of the FTC. Simulation and experimental studies are conducted in Section 5. Finally, conclusions are drawn in Section 6.

II. FAULTY INPUT-DELAYED GIMBAL SYSTEM MODELING

The mathematical representation of the controlled system has been derived in the author's previous studies [33]. It is written as follows:

$$\begin{aligned}
\dot{\boldsymbol{\varphi}} &= \boldsymbol{f}\left(\varphi_{tx}, \varphi_{ty}\right)\boldsymbol{\omega} \\
\dot{\boldsymbol{\omega}} &= \boldsymbol{B}\boldsymbol{u}(t-\tau) - \boldsymbol{K}\boldsymbol{\omega} + \boldsymbol{d} \\
\boldsymbol{f}\left(\varphi_{tx}, \varphi_{ty}\right) &= \begin{bmatrix} \cos\varphi_{tx} & -\sin\varphi_{tx} \\ \sin\varphi_{tx}/\cos\varphi_{ty} & \cos\varphi_{tx}/\cos\varphi_{ty} \end{bmatrix}, \\
\boldsymbol{K} &= \begin{bmatrix} K_{ty} & 0 \\ 0 & K_{pz} \end{bmatrix}, \quad \boldsymbol{B} = \begin{bmatrix} B_{ty} & 0 \\ 0 & B_{tz}\cos\theta \end{bmatrix}
\end{aligned} \tag{1}$$

where $\boldsymbol{\varphi} = [\,\varphi_{ty}\ \varphi_{tz}\,]^T$ denote the controlled tilt and pan rotation of the inner gimbal in Euler angles, and φ_{tx} is the uncontrolled roll angle. $\boldsymbol{\omega} = [\,\omega_{ty}\ \omega_{tz}\,]^T$ is the corresponding controlled angular rate. $\boldsymbol{u} = [\,u_y\ u_z\,]^T$ is the control signal for the actuators of the inner and outer channels, respectively. τ is the time-varying delay at the inputs, due to the use of the networked system. θ is the relative orientation between the two channels. K_{ty}, K_{pz}, B_{ty}, and B_{tz} are the system parameters. The effect of the vehicle's motions, imbalance, and constraints on the tilt and pan motions are represented by the vector $\boldsymbol{d} = \left[\,d_{ty}\ d_{tz}\,\right]^T$.

The AHRS used in the system provides twelve measurements, including accelerations, angular rates, geomagnetism, and 3D orientation. However, in the control loop of the gimbal system, only two angular rates and two Euler angles are involved. That is, the vector of measurement considered in this section is given by:

$$\boldsymbol{Y} = \left[\,\varphi_{ty}\ \ \varphi_{tz}\ \ \omega_{ty}\ \ \omega_{tz}\,\right] \tag{2}$$

Assume that the fault occurs only at the measurement of the pan angle. Accordingly, the incorrect measurement given by the faulty AHRS is:

$$\boldsymbol{Y} = \left[\,\varphi_{ty}\ \ \varphi_{tz} + f_s\ \ \omega_{ty}\ \ \omega_{tz}\,\right] \tag{3}$$

where f_s denotes the fault. Moreover, suppose that the sensor fault is generated by an exogenous signal ζ such that:

$$\dot{f}_s = -hf_s + \zeta, \quad h > 0 \tag{4}$$

By treating f_s as an extended state of the system, the description of the system with sensor fault can be derived from Eq. (1) and (4) as follows:

$$\begin{aligned} \dot{\boldsymbol{X}} &= \boldsymbol{F}(\boldsymbol{X})\boldsymbol{X} + \boldsymbol{B_X}\boldsymbol{u_\tau} + \boldsymbol{D_X}\boldsymbol{d_X} \\ \boldsymbol{Y} &= \boldsymbol{C_X}\boldsymbol{X} \end{aligned} \tag{5}$$

where:

$$\boldsymbol{X} = \left[\,\varphi_{ty}\ \varphi_{tz}\ \omega_{ty}\ \omega_{tz}\ f_s\,\right]^T,\ \boldsymbol{u_\tau} = \boldsymbol{u}\,(t-\tau),\ \boldsymbol{d_X} = \begin{bmatrix} \boldsymbol{d} \\ \zeta \end{bmatrix},$$

$$\boldsymbol{F}(\boldsymbol{X}) = \begin{bmatrix} \boldsymbol{O_2} & \boldsymbol{f}\left(\varphi_{tx}, \varphi_{ty}\right) & \boldsymbol{O_{2\times 1}} \\ \boldsymbol{O_2} & \boldsymbol{K} & \boldsymbol{O_{2\times 1}} \\ \boldsymbol{O_{1\times 4}} & & -h \end{bmatrix}, \quad \boldsymbol{B_X} = \begin{bmatrix} \boldsymbol{O_2} \\ \boldsymbol{B} \\ \boldsymbol{O_{1\times 2}} \end{bmatrix},$$

$$\boldsymbol{C_X} = \begin{bmatrix} 0 \\ 1 \\ \boldsymbol{I_4} \\ 0 \\ 0 \end{bmatrix}, \quad \boldsymbol{D_X} = \begin{bmatrix} \boldsymbol{O_{2\times 3}} \\ \boldsymbol{I_3} \end{bmatrix} \tag{6}$$

The denotation $\boldsymbol{I_n}$ is used for the identity matrix size n and $\boldsymbol{O_{m\times n}}$ is for the m-by-n zero matrix. From this new representation, some features of the system are derived, as follows:

- Firstly, the rank of the matrix $\boldsymbol{D_X}$ is equal to the rank of the matrix multiplication $\boldsymbol{C_X D_X}$. That is:

$$rank\,(\boldsymbol{C_X D_X}) = rank\,(\boldsymbol{D_X}) = 3 \tag{7}$$

- Secondly, there exists a value $\kappa > 0$ such that:

$$\|\boldsymbol{F}(\boldsymbol{X_1})\boldsymbol{X_1} - \boldsymbol{F}(\boldsymbol{X_2})\boldsymbol{X_2}\| \le \kappa\,\|\boldsymbol{X_1} - \boldsymbol{X_2}\| \tag{8}$$

III. DESIGN OF THE FAULT DETECTION AND ISOLATION

A. DESIGN OF THE ROBUST UNKNOWN INPUT OBSERVER

The objective of the UIO is to estimate the value of the system states such that the estimation errors are decoupled from the unknown inputs acting on the system. The UIO is proposed for the considered system in the following form [26], [27]:

$$\begin{aligned} \dot{\hat{\boldsymbol{X}}} &= \boldsymbol{E}\left(\boldsymbol{F}(\hat{\boldsymbol{X}})\hat{\boldsymbol{X}} + \hat{\boldsymbol{B}}_{\boldsymbol{X}}\bar{\boldsymbol{u}}_{\boldsymbol{\tau}}\right) + \boldsymbol{H}\left(\boldsymbol{Y} - \hat{\boldsymbol{Y}}\right) + \boldsymbol{Z}\dot{\boldsymbol{Y}} \\ \hat{\boldsymbol{Y}} &= \boldsymbol{C_X}\hat{\boldsymbol{X}} \end{aligned} \tag{9}$$

where $\hat{\boldsymbol{X}}$ and $\hat{\boldsymbol{Y}}$ are the estimated values of the system states and outputs, respectively. $\bar{\boldsymbol{u}}_{\boldsymbol{\tau}} = \boldsymbol{u}\,(t-\bar{\tau})$, the constant $\bar{\tau}$ is the mean delay time. $\boldsymbol{E}$, $\boldsymbol{H}$, and $\boldsymbol{Z}$ are the observer's gains to be designed.

The estimation error vector is defined as the difference between actual system states and the estimated states obtained by the UIO. From Eq. (5) and (9), the time derivative of the estimation error is obtained as follows:

$$\begin{aligned} \dot{\tilde{\boldsymbol{X}}} &= \dot{\boldsymbol{X}} - \dot{\hat{\boldsymbol{X}}} \\ &= \boldsymbol{E}\left(\boldsymbol{F}(\boldsymbol{X})\boldsymbol{X} - \boldsymbol{F}(\hat{\boldsymbol{X}})\hat{\boldsymbol{X}}\right) + (\boldsymbol{I} - \boldsymbol{Z}\boldsymbol{C_X} - \boldsymbol{E})\,\boldsymbol{B_X}\bar{\boldsymbol{u}}_{\boldsymbol{\tau}} \\ &\quad + (\boldsymbol{I} - \boldsymbol{E} - \boldsymbol{Z}\boldsymbol{C_X})\,\boldsymbol{F}(\boldsymbol{X})\boldsymbol{X} + (\boldsymbol{D_X} - \boldsymbol{Z}\boldsymbol{C_X}\boldsymbol{D_X})\,\boldsymbol{d_X} \\ &\quad + (\boldsymbol{I} - \boldsymbol{Z}\boldsymbol{C_X})\,\boldsymbol{B_X}\tilde{\boldsymbol{u}}_{\boldsymbol{\tau}} - \boldsymbol{H}\boldsymbol{C_X}\tilde{\boldsymbol{X}} \end{aligned} \tag{10}$$

with $\tilde{\boldsymbol{u}}_{\boldsymbol{\tau}} = \boldsymbol{u}_{\boldsymbol{\tau}} - \bar{\boldsymbol{u}}_{\boldsymbol{\tau}}$. As shown in this Equation, the estimated states are not only dependent on the system states and sensor fault but also the control signals and disturbances. Ideally, the estimation should be independent of $\bar{\boldsymbol{u}}_{\boldsymbol{\tau}}, \boldsymbol{d_X}$ and $\tilde{\boldsymbol{u}}_{\boldsymbol{\tau}}$. However, since there are only two variables $\boldsymbol{Z}$ and $\boldsymbol{E}$ in their three coefficients, decoupling all of these factors simultaneously is impossible. The best outcome for the UIO is that: (a) $\tilde{\boldsymbol{X}}$ is decoupled from $\bar{\boldsymbol{u}}_{\boldsymbol{\tau}}$ and $\boldsymbol{d_X}$, (b) $\tilde{\boldsymbol{X}}$ converges as the time $t \to \infty$, and (c) the influence of $\tilde{\boldsymbol{u}}_{\boldsymbol{\tau}}$ is minimized.

For condition (a), the gains $\boldsymbol{Z}$ and $\boldsymbol{E}$ are necessarily chosen such that:

$$\begin{aligned} (\boldsymbol{I} - \boldsymbol{Z}\boldsymbol{C_X} - \boldsymbol{E}) &= 0 \\ (\boldsymbol{D_X} - \boldsymbol{Z}\boldsymbol{C_X}\boldsymbol{D_X}) &= 0 \end{aligned} \tag{11}$$

A general solution of the second equation of (11) is given in the following form [26]:

$$\boldsymbol{Z} = \boldsymbol{Z_1} + \boldsymbol{T}\boldsymbol{Z_2} \tag{12}$$

where:

$$\begin{aligned} &\boldsymbol{Z_1} = \boldsymbol{D_X}\,(\boldsymbol{C_X D_X})^*,\ \boldsymbol{Z_2} = \boldsymbol{I} - \boldsymbol{C_X D_X}\,(\boldsymbol{C_X D_X})^*, \\ &(\boldsymbol{C_X D_X})^* = \left[(\boldsymbol{C_X D_X})^T\,(\boldsymbol{C_X D_X})\right]^{-1}(\boldsymbol{C_X D_X})^T \end{aligned} \tag{13}$$

$(\boldsymbol{C_X D_X})^*$ is the left pseudo-inverse matrix of $(\boldsymbol{C_X D_X})$. Additionally, $\boldsymbol{T}$ is to be designed later.

Accordingly, the gain $\boldsymbol{E}$ satisfying the first condition of Eq. (11) is obtained by:

$$\boldsymbol{E} = \boldsymbol{I} - \boldsymbol{Z_1}\boldsymbol{C_X} - \boldsymbol{T}\boldsymbol{Z_2}\boldsymbol{C_X} \tag{14}$$

Then, the dynamics of the estimation error is given in Eq. (15) and is independent of $\bar{\boldsymbol{u}}_{\boldsymbol{\tau}}$ and $\boldsymbol{d_X}$:

$$\begin{aligned} \dot{\tilde{\boldsymbol{X}}} &= \dot{\boldsymbol{X}} - \dot{\hat{\boldsymbol{X}}} \\ &= \boldsymbol{E}\left(\boldsymbol{F}(\boldsymbol{X})\boldsymbol{X} - \boldsymbol{F}(\hat{\boldsymbol{X}})\hat{\boldsymbol{X}}\right) - \boldsymbol{H}\boldsymbol{C_X}\tilde{\boldsymbol{X}} + \boldsymbol{E}\boldsymbol{B_X}\tilde{\boldsymbol{u}}_{\boldsymbol{\tau}} \end{aligned} \tag{15}$$

For the convergence of the estimation error as in the condition (b), the following Lyapunov function candidate is taken into consideration:

$$V_{UIO} = \tilde{\boldsymbol{X}}^{\boldsymbol{T}} \boldsymbol{P} \tilde{\boldsymbol{X}} \tag{16}$$

$\boldsymbol{P}$ is symmetric and positive definite. The time derivative of V_{UIO} satisfies the following inequality:

$$\dot{V}_{UIO} \leq \tilde{\boldsymbol{X}}^{T} \left(-\boldsymbol{C}_{\boldsymbol{X}}^{T} \boldsymbol{H}^{T} \boldsymbol{P} - \boldsymbol{P} \boldsymbol{H} \boldsymbol{C}_{\boldsymbol{X}} + \boldsymbol{E}^{T} \boldsymbol{P} \boldsymbol{P} \boldsymbol{E} + \kappa \boldsymbol{I} + \frac{1}{\gamma^{2}} \bar{\boldsymbol{B}}_{\boldsymbol{X}}^{T} \boldsymbol{E}^{T} \boldsymbol{P} \boldsymbol{P} \boldsymbol{E} \bar{\boldsymbol{B}}_{\boldsymbol{X}} \right) \tilde{\boldsymbol{X}} + \gamma^{2} \tilde{\boldsymbol{u}}_{\boldsymbol{\tau}}^{T} \underline{\boldsymbol{B}}_{\boldsymbol{X}}^{T} \underline{\boldsymbol{B}}_{\boldsymbol{X}} \tilde{\boldsymbol{u}}_{\boldsymbol{\tau}} \tag{17}$$

where $\underline{\boldsymbol{B}}_{\boldsymbol{X}} = \begin{bmatrix} 1 & 0 \\ 0 & \cos\theta \end{bmatrix}$, $\bar{\boldsymbol{B}}_{\boldsymbol{X}} \underline{\boldsymbol{B}}_{\boldsymbol{X}} = \boldsymbol{B}_{\boldsymbol{X}}$, and γ is a positive constant to be minimized. The proof of the inequality is given in Appendix A.

Now, consider another inequality given by:

$$\dot{V}_{UIO} + \tilde{\boldsymbol{X}}^{T} \tilde{\boldsymbol{X}} - \gamma^{2} \tilde{\boldsymbol{u}}_{\boldsymbol{\tau}}^{T} \underline{\boldsymbol{B}}_{\boldsymbol{X}}^{T} \underline{\boldsymbol{B}}_{\boldsymbol{X}} \tilde{\boldsymbol{u}}_{\boldsymbol{\tau}} \leq 0 \tag{18}$$

The feasibility of the inequality results in the boundedness of the $\boldsymbol{L_2}$ gain of the system defined as [34]:

$$\sup_{\|\underline{\boldsymbol{B}}_{\boldsymbol{X}} \tilde{\boldsymbol{u}}_{\boldsymbol{\tau}}\|_2 \neq 0} \frac{\left\| \tilde{\boldsymbol{X}} \right\|_2}{\left\| \underline{\boldsymbol{B}}_{\boldsymbol{X}} \tilde{\boldsymbol{u}}_{\boldsymbol{\tau}} \right\|_2} \leq \gamma \tag{19}$$

where γ is the upper bound on the $\boldsymbol{L_2}$ gain. Minimizing γ results in the smallest boundedness of the estimation error. Thus, condition (c) of the UIO is satisfied.

Following the Schur complement, Eq. (18) is equivalent to:

$$\begin{bmatrix} -\boldsymbol{C}_{\boldsymbol{X}}^{T} \boldsymbol{H}^{T} \boldsymbol{P} - \boldsymbol{P} \boldsymbol{H} \boldsymbol{C}_{\boldsymbol{X}} + (\kappa + 1) \boldsymbol{I} & \boldsymbol{P} \boldsymbol{E} & \boldsymbol{P} \boldsymbol{E} \bar{\boldsymbol{B}}_{\boldsymbol{X}} \\ \boldsymbol{E}^{T} \boldsymbol{P} & -\boldsymbol{I} & \boldsymbol{O} \\ \bar{\boldsymbol{B}}_{\boldsymbol{X}}^{T} \boldsymbol{E}^{T} \boldsymbol{P} & \boldsymbol{O} & -\gamma^{2} \boldsymbol{I} \end{bmatrix} \leq 0 \tag{20}$$

This is a bilinear matrix inequality (BMI), which is hard to solve. Therefore, let some variable changes be made as in Eq. (21) so that the linear matrix inequality (LMI) in Eq. (22) is obtained:

$$\boldsymbol{H} = (\boldsymbol{I} + \boldsymbol{M}_{H}) \boldsymbol{C}_{\boldsymbol{X}}^{*}, \; \boldsymbol{C}_{\boldsymbol{X}}^{*} = \boldsymbol{C}_{\boldsymbol{X}}^{T} \left(\boldsymbol{C}_{\boldsymbol{X}} \boldsymbol{C}_{\boldsymbol{X}}^{T} \right)^{-1}, \quad \boldsymbol{P}_{M} = \boldsymbol{P} \boldsymbol{M}_{H}, \; \boldsymbol{P}_{T} = \boldsymbol{P} \boldsymbol{T} \tag{21}$$

$$\begin{bmatrix} -2\boldsymbol{P} - \boldsymbol{P}_{M} - \boldsymbol{P}_{M}^{T} + (\kappa+1) \boldsymbol{I} & \boldsymbol{J}_1 & \boldsymbol{J}_2 \\ \boldsymbol{J}_1^{T} & -\boldsymbol{I} & \boldsymbol{O} \\ \boldsymbol{J}_2^{T} & \boldsymbol{O} & -\gamma^{2} \boldsymbol{I} \end{bmatrix} \leq 0 \tag{22}$$

where

$$\begin{aligned} \boldsymbol{J}_1 &= \boldsymbol{P} (\boldsymbol{I} - \boldsymbol{Z_1} \boldsymbol{C}_{\boldsymbol{X}}) - \boldsymbol{P}_{\boldsymbol{T}} \boldsymbol{Z_2} \boldsymbol{C}_{\boldsymbol{X}} \\ \boldsymbol{J}_2 &= \boldsymbol{P} (\boldsymbol{I} - \boldsymbol{Z_1} \boldsymbol{C}_{\boldsymbol{X}}) \bar{\boldsymbol{B}}_{\boldsymbol{X}} - \boldsymbol{P}_{\boldsymbol{T}} \boldsymbol{Z_2} \boldsymbol{C}_{\boldsymbol{X}} \bar{\boldsymbol{B}}_{\boldsymbol{X}} \end{aligned} \tag{23}$$

If there exist γ, $\boldsymbol{P}$, $\boldsymbol{P}_{M}$, and $\boldsymbol{P}_{T}$ such that the feasibility of the LMI in Eq. (22) is preserved, the designed UIO is stable. The estimation error is bounded by the $\boldsymbol{L_2}$ gain condition in Eq. (19).

B. FAULT DETECTION MECHANISM

Given the measurement from the AHRS and the observation by the UIO, the fault is fully identified. The estimated value of the fault, namely $\hat{f}_s$, is given by the 5$^{\text{th}}$ element of the estimated state vector. However, the UIO can only preserve the boundedness of the estimation error rather than the asymptotic stability. Thus, to reduce the false alarm rate of the fault detection, the fault alarm is triggered by a relay mechanism with hysteresis, as in Fig. 1, where f_{th_l} and f_{th_u} are the lower and upper thresholds, respectively. When $\left|\hat{f}_s\right| > f_{th\_u}$, the fault alarm is enabled, which means the sensor fault is detected. When $\left|\hat{f}_s\right| < f_{th\_l}$, the fault alarm goes off, and the control system assumes there is no fault. When the amplitude of the estimated fault is between the two levels, the fault alarm retains its value. Therefore, this mechanism preserves the robust fault detection even with the noisy estimation.

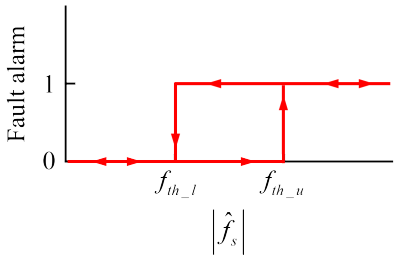

FIGURE 1. Fault detection mechanism.

Accordingly, the sensor measurement cannot be trusted in the presence of the fault alarm. Then, the pan rotation fed to the controller should be switched to the observation $\hat{\varphi}_{tz}$ by the UIO as follows:

$$\bar{\varphi}_{tz} = \begin{cases} \hat{\varphi}_{tz} & \text{if} \quad \text{Fault alarm} = 1 \\ \varphi_{tz} & \text{if} \quad \text{Fault alarm} = 0 \end{cases} \tag{24}$$

C. DISTURBANCE ESTIMATION

For the effect of the disturbances and delay on the system, let us propose an estimation as follows:

$$\hat{\boldsymbol{d}}_{\boldsymbol{X}} = (\boldsymbol{C}_{\boldsymbol{X}} \boldsymbol{D}_{\boldsymbol{X}})^{*} \dot{\boldsymbol{Y}} - \boldsymbol{W} \left(\boldsymbol{F} \left(\hat{\boldsymbol{X}} \right) \boldsymbol{X} \hat{+} \boldsymbol{B}_{\boldsymbol{X}} \bar{\boldsymbol{u}}_{\boldsymbol{\tau}} \right) \tag{25}$$

with $\boldsymbol{W}$ a matrix to be designed. Substituting $\dot{\boldsymbol{Y}}$ from the system model in Eq. (5) and $\hat{\boldsymbol{X}}$ estimated by the UIO from Eq. (9) into Eq. (25) yields the following:

$$\begin{aligned} \hat{\boldsymbol{d}}_{\boldsymbol{X}} = \boldsymbol{d}_{\boldsymbol{X}} &+ (\boldsymbol{C}_{\boldsymbol{X}} \boldsymbol{D}_{\boldsymbol{X}})^{*} \boldsymbol{C}_{\boldsymbol{X}} \boldsymbol{B}_{\boldsymbol{X}} \tilde{\boldsymbol{u}}_{\boldsymbol{\tau}} + (\boldsymbol{C}_{\boldsymbol{X}} \boldsymbol{D}_{\boldsymbol{X}})^{*} \boldsymbol{C}_{\boldsymbol{X}} \boldsymbol{F} (\boldsymbol{X}) \boldsymbol{X} \\ &- \boldsymbol{W} \boldsymbol{F} (\hat{\boldsymbol{X}}) \hat{\boldsymbol{X}} + \left((\boldsymbol{C}_{\boldsymbol{X}} \boldsymbol{D}_{\boldsymbol{X}})^{*} \boldsymbol{C}_{\boldsymbol{X}} - \boldsymbol{W} \right) \boldsymbol{B}_{\boldsymbol{X}} \bar{\boldsymbol{u}}_{\boldsymbol{\tau}} \end{aligned} \tag{26}$$

By choosing $\boldsymbol{W} = (\boldsymbol{C}_{\boldsymbol{X}} \boldsymbol{D}_{\boldsymbol{X}})^{*} \boldsymbol{C}_{\boldsymbol{X}}$, we obtain:

$$\hat{\boldsymbol{d}}_{\boldsymbol{X}} = \boldsymbol{d}_{\boldsymbol{X}} + \boldsymbol{W} \boldsymbol{B}_{\boldsymbol{X}} \tilde{\boldsymbol{u}}_{\boldsymbol{\tau}} + \boldsymbol{W} \left(\boldsymbol{F}(\boldsymbol{X}) \boldsymbol{X} - \boldsymbol{F}(\hat{\boldsymbol{X}}) \hat{\boldsymbol{X}} \right) \tag{27}$$

Hence, $\left\| \hat{\boldsymbol{d}}_{\boldsymbol{X}} - \boldsymbol{d}_{\boldsymbol{X}} - \boldsymbol{W} \boldsymbol{B}_{\boldsymbol{X}} \tilde{\boldsymbol{u}}_{\boldsymbol{\tau}} \right\| \leq \kappa \boldsymbol{W} \left\| \tilde{\boldsymbol{X}} \right\|$. Thus, $\hat{\boldsymbol{d}}_{\boldsymbol{X}}$ estimates the total effect of the disturbance, $\boldsymbol{d}_{\boldsymbol{X}}$, and the time-varying delay, presented by $\boldsymbol{W} \boldsymbol{B}_{\boldsymbol{X}} \tilde{\boldsymbol{u}}_{\boldsymbol{\tau}}$, with a small error.

IV. FAULT-TOLERANT CONTROL SYSTEM DESIGN

The proposed control law is based on the integral sliding mode method [35]. In this method, the control law $\boldsymbol{u}$ consists of two parts: the control law $\boldsymbol{u_0}$ achieves the control objective for the nominal system, and the robust control law $\boldsymbol{u_d}$ ensures the sliding motion occurs on an integral type sliding manifold. The design of each part is respectively presented in this section.

A. BACKSTEPPING-BASED CONTROL LAW FOR THE NOMINAL SYSTEM MODEL

The fundamental objective of a tracking system using gimbaled mechanisms is to stabilize the LOS and steer it to follow the desired target. This is equivalent to the convergence of the tracking error $\boldsymbol{e_\varphi}$ and the stabilization error $\boldsymbol{e_\omega}$, which are defined as follows:

$$\begin{aligned} \boldsymbol{e_\varphi} &= \boldsymbol{\varphi}_d - \boldsymbol{\varphi} \\ \boldsymbol{e_\omega} &= \boldsymbol{\Lambda e_\varphi} + \dot{\boldsymbol{\varphi}}_d - \boldsymbol{f}\left(\varphi_{tx}, \varphi_{ty}\right)\boldsymbol{\omega} \end{aligned} \tag{28}$$

with $\boldsymbol{\Lambda}$ a diagonal positive definite matrix. Referring to the decision of the fault detection mechanism, the feedback value of the pan position is $\bar{\varphi}_{tz}$. The control errors can be rewritten as:

$$\begin{aligned} \boldsymbol{e_\varphi} &= \bar{\boldsymbol{e}}_{\boldsymbol{\varphi}} - \tilde{\boldsymbol{\varphi}} \\ \boldsymbol{e_\omega} &= \bar{\boldsymbol{e}}_{\boldsymbol{\omega}} - \boldsymbol{\Lambda}\tilde{\boldsymbol{\varphi}} \end{aligned} \tag{29}$$

where

$$\begin{aligned} \bar{\boldsymbol{e}}_{\boldsymbol{\varphi}} &= \boldsymbol{\varphi}_d - \begin{bmatrix} \varphi_{ty} \\ \bar{\varphi}_{tz} \end{bmatrix}, \quad \tilde{\boldsymbol{\varphi}} = \begin{bmatrix} 0 \\ \varphi_{tz} - \bar{\varphi}_{tz} \end{bmatrix}, \\ \bar{\boldsymbol{e}}_{\boldsymbol{\omega}} &= \boldsymbol{\Lambda}\bar{\boldsymbol{e}}_{\boldsymbol{\varphi}} + \dot{\boldsymbol{\varphi}}_d - \boldsymbol{f}\left(\varphi_{tx}, \varphi_{ty}\right)\boldsymbol{\omega} \end{aligned} \tag{30}$$

The nominal model of the system is obtained by removing non-ideal factors, including the disturbances, delay, and fault, out of the system representation. That is:

$$\begin{aligned} \dot{\boldsymbol{\varphi}} &= \boldsymbol{f}\left(\varphi_{tx}, \varphi_{ty}\right)\boldsymbol{\omega} \\ \dot{\boldsymbol{\omega}} &= \boldsymbol{Bu} - \boldsymbol{K\omega} \end{aligned} \tag{31}$$

Then, the dynamics of the control error derived for the nominal system is given by:

$$\begin{aligned} \dot{\boldsymbol{e}}_{\boldsymbol{\varphi}} &= -\boldsymbol{\Lambda e_\varphi} + \boldsymbol{e_\omega} \\ \dot{\boldsymbol{e}}_{\boldsymbol{\omega}} &= \ddot{\boldsymbol{\varphi}}_d - \boldsymbol{\Lambda}^2\boldsymbol{e_\varphi} + \boldsymbol{\Lambda e_\omega} - \frac{\partial}{\partial t}\boldsymbol{f}\left(\varphi_{tx}, \varphi_{ty}\right)\boldsymbol{\omega} \\ &\quad - \boldsymbol{f}\left(\varphi_{tx}, \varphi_{ty}\right)(\boldsymbol{Bu} - \boldsymbol{K\omega}) \end{aligned} \tag{32}$$

Consider the quadratic Lyapunov function candidate given by Eq. (33), it is easily seen that the desired dynamics of the error terms obtained as in Eq. (34) accomplish the control objectives.

$$V = \boldsymbol{e}_{\boldsymbol{\varphi}}^{\boldsymbol{T}}\boldsymbol{e_\varphi} + \boldsymbol{e}_{\boldsymbol{\omega}}^{\boldsymbol{T}}\boldsymbol{e_\omega} \tag{33}$$

$$\boldsymbol{e_\omega} = -\boldsymbol{e_\varphi} - \boldsymbol{\Gamma e_\omega} \tag{34}$$

with $\boldsymbol{\Gamma}$ a diagonal positive definite matrix.

Comparing Eq. (32) to Eq. (34), the control law achieving the control objectives for the nominal system is easily obtained. Additionally, in the fault-free system, $\bar{\varphi}_{tz} = \varphi_{tz}$, then $\boldsymbol{e_\varphi} = \bar{\boldsymbol{e}}_{\boldsymbol{\varphi}}$ and $\boldsymbol{e_\omega} = \bar{\boldsymbol{e}}_{\boldsymbol{\omega}}$. Thus, the control law is written as follows:

$$\begin{aligned} \boldsymbol{Bu_0} = \boldsymbol{K\omega} + \left[\boldsymbol{f}\left(\varphi_{tx}, \varphi_{ty}\right)\right]^{-1}\Big[&\ddot{\boldsymbol{\varphi}}_{\boldsymbol{d}} + \left(\boldsymbol{I} - \boldsymbol{\Lambda}^{\boldsymbol{2}}\right)\bar{\boldsymbol{e}}_{\boldsymbol{\varphi}} \\ &- \frac{\partial}{\partial t}\boldsymbol{f}\left(\varphi_{tx}, \varphi_{ty}\right)\boldsymbol{\omega} + (\boldsymbol{\Gamma} + \boldsymbol{\Lambda})\,\bar{\boldsymbol{e}}_{\boldsymbol{\omega}}\Big] \end{aligned} \tag{35}$$

with $\left[\boldsymbol{f}\left(\varphi_{tx}, \varphi_{ty}\right)\right]^{-1} = \dfrac{1}{\cos\varphi_{ty}}\begin{bmatrix} \cos\varphi_{tx} & -\sin\varphi_{tx} \\ \cos\varphi_{ty} & \cos\varphi_{ty} \\ \sin\varphi_{tx} & \cos\varphi_{tx} \end{bmatrix}$.

B. ROBUST INTEGRAL SUPER-TWISTING SLIDING MODE FAULT-TOLERANT CONTROL

Let the sliding manifold be chosen as follows:

$$\begin{aligned} \boldsymbol{s} &= \dot{\boldsymbol{e}}_{\boldsymbol{\varphi}} + (\boldsymbol{\Gamma} + \boldsymbol{\Lambda})\,\bar{\boldsymbol{e}}_{\boldsymbol{\varphi}} + (\boldsymbol{I} + \boldsymbol{\Gamma\Lambda})\int_0^t \bar{\boldsymbol{e}}_{\boldsymbol{\varphi}}(\iota)\,d\iota \\ &= \dot{\boldsymbol{e}}_{\boldsymbol{\varphi}} + (\boldsymbol{\Gamma} + \boldsymbol{\Lambda})\,\boldsymbol{e_\varphi} + (\boldsymbol{I} + \boldsymbol{\Gamma\Lambda})\int_0^t \boldsymbol{e_\varphi}(\iota)\,d\iota \\ &\quad + (\boldsymbol{\Gamma} + \boldsymbol{\Lambda})\,\tilde{\boldsymbol{\varphi}} + (\boldsymbol{I} + \boldsymbol{\Gamma\Lambda})\int_0^t \tilde{\boldsymbol{\varphi}}(\iota)\,d\iota \end{aligned} \tag{36}$$

where $\dot{\boldsymbol{e}}_{\boldsymbol{\varphi}} = \dot{\boldsymbol{\varphi}}_{\boldsymbol{d}} - \boldsymbol{f}\left(\varphi_{tx}, \varphi_{ty}\right)\boldsymbol{\omega}$ derived from Eq. (28). The time derivative of the manifold is given by:

$$\begin{aligned} \dot{\boldsymbol{s}} &= \ddot{\boldsymbol{e}}_{\boldsymbol{\varphi}} + (\boldsymbol{\Gamma} + \boldsymbol{\Lambda})\,\dot{\boldsymbol{e}}_{\boldsymbol{\varphi}} + (\boldsymbol{I} + \boldsymbol{\Gamma\Lambda})\,\boldsymbol{e_\varphi} + (\boldsymbol{\Gamma} + \boldsymbol{\Lambda})\,\dot{\tilde{\boldsymbol{\varphi}}} \\ &\quad + (\boldsymbol{I} + \boldsymbol{\Gamma\Lambda})\left(\tilde{\boldsymbol{\varphi}} - \tilde{\boldsymbol{\varphi}}_{\boldsymbol{0}}\right) \\ &= \ddot{\boldsymbol{\varphi}}_{\boldsymbol{d}} - \frac{\partial}{\partial t}\boldsymbol{f}\left(\varphi_{tx}, \varphi_{ty}\right)\boldsymbol{\omega} - \boldsymbol{f}\left(\varphi_{tx}, \varphi_{ty}\right)(\boldsymbol{Bu}_{\boldsymbol{\tau}} - \boldsymbol{K\omega} + \boldsymbol{d}) \\ &\quad + (\boldsymbol{\Gamma} + \boldsymbol{\Lambda})\,\boldsymbol{e_\omega} + \left(\boldsymbol{I} - \boldsymbol{\Lambda}^2\right)\boldsymbol{e_\varphi} + (\boldsymbol{I} + \boldsymbol{\Gamma\Lambda})\,\tilde{\boldsymbol{\varphi}} + (\boldsymbol{\Gamma} + \boldsymbol{\Lambda})\,\dot{\tilde{\boldsymbol{\varphi}}} \\ &\quad - (\boldsymbol{I} + \boldsymbol{\Gamma\Lambda})\,\tilde{\boldsymbol{\varphi}}_{\boldsymbol{0}} \end{aligned} \tag{37}$$

with $\tilde{\boldsymbol{\varphi}}_{\boldsymbol{0}} = \tilde{\boldsymbol{\varphi}}(t_0)$. Now, the delayed control law can be expressed by:

$$\boldsymbol{Bu}_{\boldsymbol{\tau}} = \boldsymbol{Bu_0} + \boldsymbol{Bu_d} - \boldsymbol{e}_{\boldsymbol{\tau}} \tag{38}$$

where $\boldsymbol{Bu_0}$ was designed in Eq. (35) and the network disturbance is $\boldsymbol{e}_{\boldsymbol{\tau}} = \boldsymbol{Bu} - \boldsymbol{Bu}_{\boldsymbol{\tau}}$. Then, the time derivative of the manifold becomes:

$$\dot{\boldsymbol{s}} = -\boldsymbol{f}\left(\varphi_{tx}, \varphi_{ty}\right)(\boldsymbol{Bu_d} - \boldsymbol{e}_{\boldsymbol{\tau}} + \boldsymbol{d}) + (\boldsymbol{\Gamma} + \boldsymbol{\Lambda})\,\dot{\tilde{\boldsymbol{\varphi}}} - (\boldsymbol{I} + \boldsymbol{\Gamma\Lambda})\,\tilde{\boldsymbol{\varphi}}_0 \tag{39}$$

Applying the Super-Twisting algorithm, the robust term $\boldsymbol{u_d}$ of the control law can be proposed by the following continuous equation:

$$\begin{aligned} \boldsymbol{Bu_d} = \left[\boldsymbol{f}\left(\varphi_{tx}, \varphi_{ty}\right)\right]^{-1}\Bigg(&\boldsymbol{G}_1\begin{bmatrix} s_1^{1/2}\mathrm{sign}\,(s_1) \\ s_2^{1/2}\mathrm{sign}\,(s_2) \end{bmatrix} \\ &+ \boldsymbol{G}_2\int_0^t \begin{bmatrix} \mathrm{sign}\,(s_1) \\ \mathrm{sign}\,(s_2) \end{bmatrix} d\iota\Bigg) - \hat{\boldsymbol{d}} \end{aligned} \tag{40}$$

where $[\, s_1 \;\; s_2 \,]^T = \boldsymbol{s}$. $\boldsymbol{G_1}$ and $\boldsymbol{G_2}$ are the controller matrices, which are diagonal positive definite. $\hat{\boldsymbol{d}}$ are the first two elements of the estimated disturbance $\hat{\boldsymbol{d}}_{\boldsymbol{X}}$ given in Eq. (25). With the proposed $\boldsymbol{u_d}$, the time derivative $\dot{\boldsymbol{s}}$ becomes:

$$\dot{\boldsymbol{s}} = -\boldsymbol{G}_1 \begin{bmatrix} s_1^{1/2}\text{sign}\,(s_1) \\ s_2^{1/2}\text{sign}\,(s_2) \end{bmatrix} - \boldsymbol{G}_2 \int_0^t \begin{bmatrix} \text{sign}\,(s_1) \\ \text{sign}\,(s_2) \end{bmatrix} d\iota + \boldsymbol{\varepsilon} \quad (41)$$

where

$$\boldsymbol{\varepsilon} = -\boldsymbol{f}\left(\varphi_{tx}, \varphi_{ty}\right)\left(-\hat{\boldsymbol{d}} + \boldsymbol{d} - \boldsymbol{e_\tau}\right) + (\boldsymbol{\Gamma} + \boldsymbol{\Lambda})\,\dot{\tilde{\boldsymbol{\varphi}}} - (\boldsymbol{I} + \boldsymbol{\Gamma}\boldsymbol{\Lambda})\,\tilde{\boldsymbol{\varphi}}_0.$$

The vector $\boldsymbol{\varepsilon}$ can be considered as the remaining influence of matched and unmatched disturbances that are not taken into account in the proposed control law. Thanks to the UIO's estimation, $\boldsymbol{\varepsilon}$ is a bounded vector. The conditions for the sliding manifold in the form of Eq. (41) being stable have been proved in previous studies, such as in [36]–[38]. In particular, Seeber and Horn ([36]) suggested the choice of the controller gains $\boldsymbol{G_1}$ and $\boldsymbol{G_2}$ to preserve the finite-time stability of the system. The block diagram of the fault-tolerant control system is illustrated in Fig. 2.

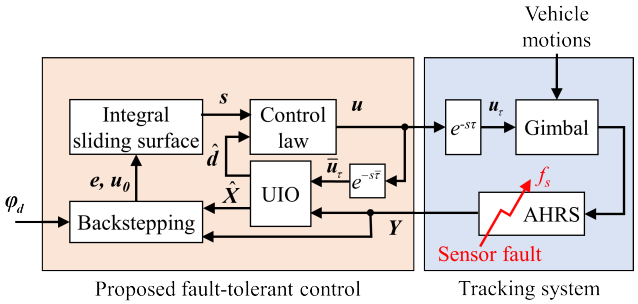

FIGURE 2. Configuration of the proposed fault-tolerant control system.

On the other hand, the integral term in the control law ensures zero steady-state errors; however, the buildup in the integrator can lead to large overshoots and long settling times. Then, the integral term $\bar{\boldsymbol{z}}_{\boldsymbol{\varphi}} = \int_0^t \bar{\boldsymbol{e}}_{\boldsymbol{\varphi}}(\iota)\, d\iota$ in the sliding manifold is modified as follows [39], [40]:

$$\begin{aligned} \dot{\bar{\boldsymbol{z}}}_{\boldsymbol{\varphi}} &\approx (\boldsymbol{\Gamma} + \boldsymbol{\Lambda})^{-1}\left[-(\boldsymbol{I} + \boldsymbol{\Gamma}\boldsymbol{\Lambda})\,\bar{\boldsymbol{z}}_{\boldsymbol{\varphi}} + \sigma\,\text{sat}\left(\frac{\boldsymbol{s} - \dot{\boldsymbol{e}}_{\boldsymbol{\varphi}}}{\sigma}\right)\right] \\ \boldsymbol{s} &= \dot{\boldsymbol{e}}_{\boldsymbol{\varphi}} + (\boldsymbol{\Gamma} + \boldsymbol{\Lambda})\,\bar{\boldsymbol{e}}_{\boldsymbol{\varphi}} + (\boldsymbol{I} + \boldsymbol{\Gamma}\boldsymbol{\Lambda})\,\bar{\boldsymbol{z}}_{\boldsymbol{\varphi}} \end{aligned} \quad (42)$$

sat $(\cdot)$ denotes the saturation function. One can easily see that inside the boundary of the saturation function, $\dot{\bar{\boldsymbol{z}}}_{\boldsymbol{\varphi}} = \bar{\boldsymbol{e}}_{\boldsymbol{\varphi}}$. Above the positive boundary, each element of $\dot{\bar{\boldsymbol{z}}}_{\boldsymbol{\varphi}}$ is always smaller than the corresponding one of the $\bar{\boldsymbol{e}}_{\boldsymbol{\varphi}}$. In contrast, below the negative boundary, $\dot{\bar{\boldsymbol{z}}}_{\boldsymbol{\varphi}} > \bar{\boldsymbol{e}}_{\boldsymbol{\varphi}}$. Thus, the modified expression in Eq. (42) ensures that the integral action takes place completely only inside the function's boundary. Large overshoots can be avoided.

In addition, chattering is well known as one of the main disadvantages of sliding mode controllers. It has been shown that this effect is mainly caused by unmodelled cascade dynamics which increase the system's relative degree and perturb the ideal sliding mode existing in the system [35]. By the integrators, the Super-Twisting algorithm is continuous, and the integral sliding mode control law is able to attenuate chattering in a relative degree one system. In order to reduce the influence of higher relative degrees, the proposed control law is calculated from a continuous signum-like function instead of the sign function.

$$\text{sign}(s_i) \approx \frac{s_i}{|s_i| + \delta_i} \quad (43)$$

with δ_i a positive constant. Unfortunately, the best outcome for the system is only uniformly ultimate boundedness instead of asymptotic stability. The boundedness of the control error is given in Appendix B.

V. SIMULATIONS AND EXPERIMENTAL STUDIES

In this section, simulations and experiments were conducted for validating the proposed UIO and FTC scheme. The parameters of the UIO were obtained by solving the LMI (22). With $\gamma = 0.1$, $\kappa = 200$ and the system's parameters given in [33], the LMI is feasible. The solutions were derived with the Robust Control Toolbox in Matlab, and the observer's gains are as in Table 1. Additionally, the lower and upper thresholds of the UIO were set at 2[deg] and 3[deg], respectively. The tuned controller's gains are also introduced in the same table. The sampling time was at 0.02[s], while the communication delay varied from the smallest delay equal to the sampling time and the largest value of 0.2[s]. The mean delay time was 0.06[s], as experimentally identified. The super-twisting sliding mode control (STSMC) and the time-delay compensation backstepping (TDC-Backstep) control from the previous study [33] were also taken into comparison with the proposed fault-tolerant control.

A. SIMULATION STUDIES

For reliable validations, two scenarios were simulated: without and with motions of the vehicle carrying the system. The sensor fault in these simulations was assumed as follows:

$$f_s = -\int_0^t (a\omega_{tz}(\iota) + b)\, d\iota \quad (44)$$

which denoted that the faulty yaw drift phenomenon behaved similarly to the integration of the sensitivity error and bias of the gyroscope in the AHRS. a and b are constant values.

The simulation results of the former scenario are depicted in Fig. 3. The time-varying delay of the network is given in Fig. 3a, and the trajectory of the tracked target is given in Fig. 3c. As seen in Fig. 3b, the proposed UIO estimated accurately the fault, even in the presence of time-varying delay. At 52[s], the amplitude of the estimated fault became greater than the upper threshold, so the fault alarm was set. The fault was confirmed for the rest of the time because the estimated value was kept higher than the lower threshold.

The actual rotations of the inner gimbal are shown in Fig. 3c, and the corresponding tracking errors are

TABLE 1. Control system parameters.

Controller's gains	$\boldsymbol{\Lambda} = \begin{bmatrix} 25 & 0 \\ 0 & 35 \end{bmatrix}, \boldsymbol{\Gamma} = \begin{bmatrix} 2.38 & 0 \\ 0 & 2.6 \end{bmatrix}, \delta = 5,$ $\boldsymbol{G}_1 = \begin{bmatrix} 10.607 & 0 \\ 0 & 10.607 \end{bmatrix}, \boldsymbol{G}_2 = \begin{bmatrix} 55 & 0 \\ 0 & 55 \end{bmatrix}$
UIO's gains	$\boldsymbol{Z} = \begin{bmatrix} 1 & 0 & 0 & 0 \\ 0 & 0 & 0 & 0 \\ 0 & 0 & 1 & 0 \\ 0 & 0 & 0 & 1 \\ 0 & 1 & 0 & 0 \end{bmatrix}, \boldsymbol{E} = \begin{bmatrix} 0 & 0 & 0 & 0 & 0 \\ 0 & 1 & 0 & 0 & 0 \\ 0 & 0 & 0 & 0 & 0 \\ 0 & 0 & 0 & 0 & 0 \\ 0 & -1 & 0 & 0 & 0 \end{bmatrix},$ $\boldsymbol{P} = \begin{bmatrix} 6.0373 & 0 & 0 & 0 & 0 \\ 0 & 3.4159 & 0 & 0 & 2.6215 \\ 0 & 0 & 6.0373 & 0 & 0 \\ 0 & 0 & 0 & 6.0373 & 0 \\ 0 & 2.6215 & 0 & 0 & 3.4159 \end{bmatrix},$ $\boldsymbol{H} = \begin{bmatrix} 17.1464 & 0 & 0 & 0 \\ 0 & 8.6592 & 0 & 0 \\ 0 & 0 & 17.1464 & 0 \\ 0 & 0 & 0 & 17.1464 \\ 0 & 8.4872 & 0 & 0 \end{bmatrix},$ $\boldsymbol{W} = \begin{bmatrix} 0 & 0 & 1 & 0 & 0 \\ 0 & 0 & 0 & 1 & 0 \\ 0 & 1 & 0 & 0 & 1 \end{bmatrix}$

illustrated in Fig. 3d. For the tilt rotation, all control systems followed the trajectory properly. The proposed fault-tolerant control system resulted in the smallest transient and steady-state errors compared to the two others. The TDC-Backstep gave the worst transient response and the STSMC recorded the largest steady-state error. The reasons were given in the previous study [33]. On the other hand, the pan rotation performed by the STSMC and TDC-Backstep failed to follow the desired reference, due to the sensor fault in the measurement of this rotation. Before the fault alarm was on, the proposed fault-tolerant control had relied on the sensor feedback, so that the actual rotation was also diverse from the reference value. After the 52nd second, the outer gimbal was controlled with the feedback from the estimated pan angle from the UIO. The rotation was corrected and followed the desired trajectory. Thus, the effectiveness of the proposed system is validated.

One of the worst-case practical scenarios was considered in the second simulation, as depicted in Fig. 4. Besides the time delay, the controlled system was also influenced by the disturbances caused by the motions of the vehicle carrying the system. These motions are represented by multi-frequency sinusoids, as in Fig. 4a. Fortunately, the UIO once again estimated properly the fault, even in the presence of these significant disturbances. Therefore, the UIO's estimations were

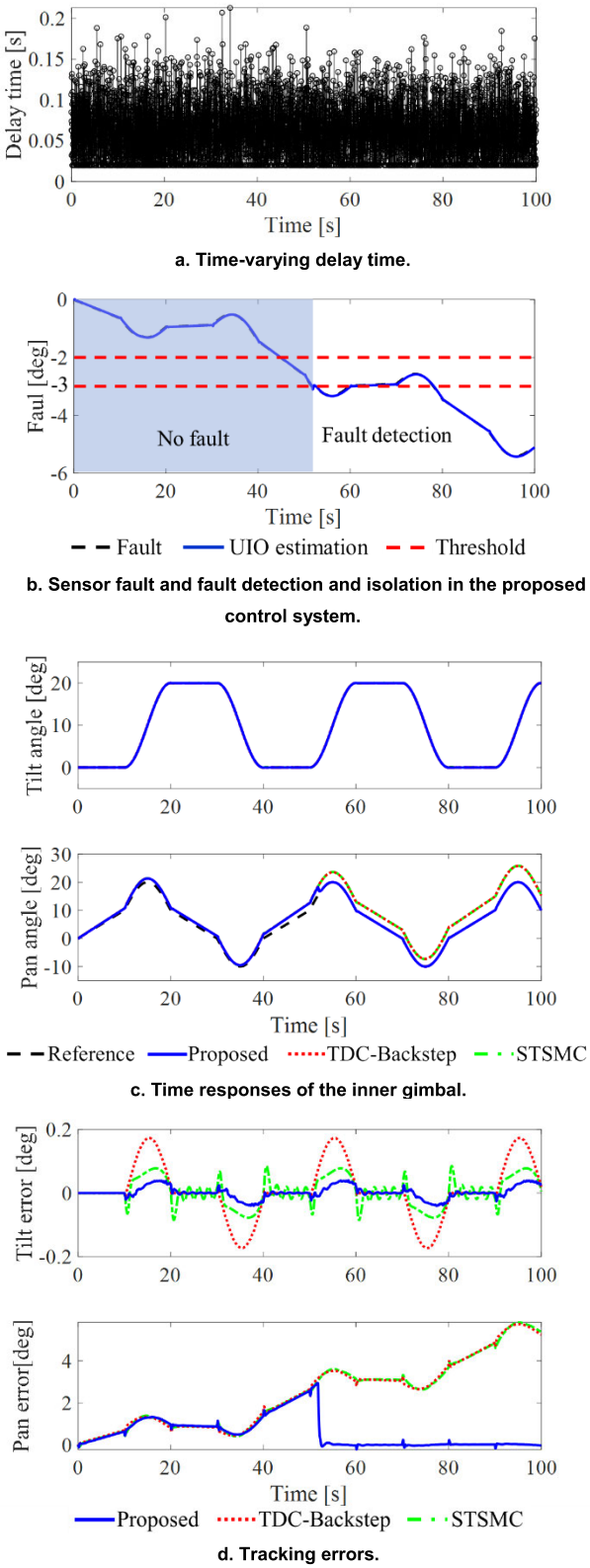

FIGURE 3. Simulation results in the first scenario.

decoupled not only from the delay time but also the disturbances. The fault estimation was then used with the STSMC and the TDC-Backstep to be compared to the proposed

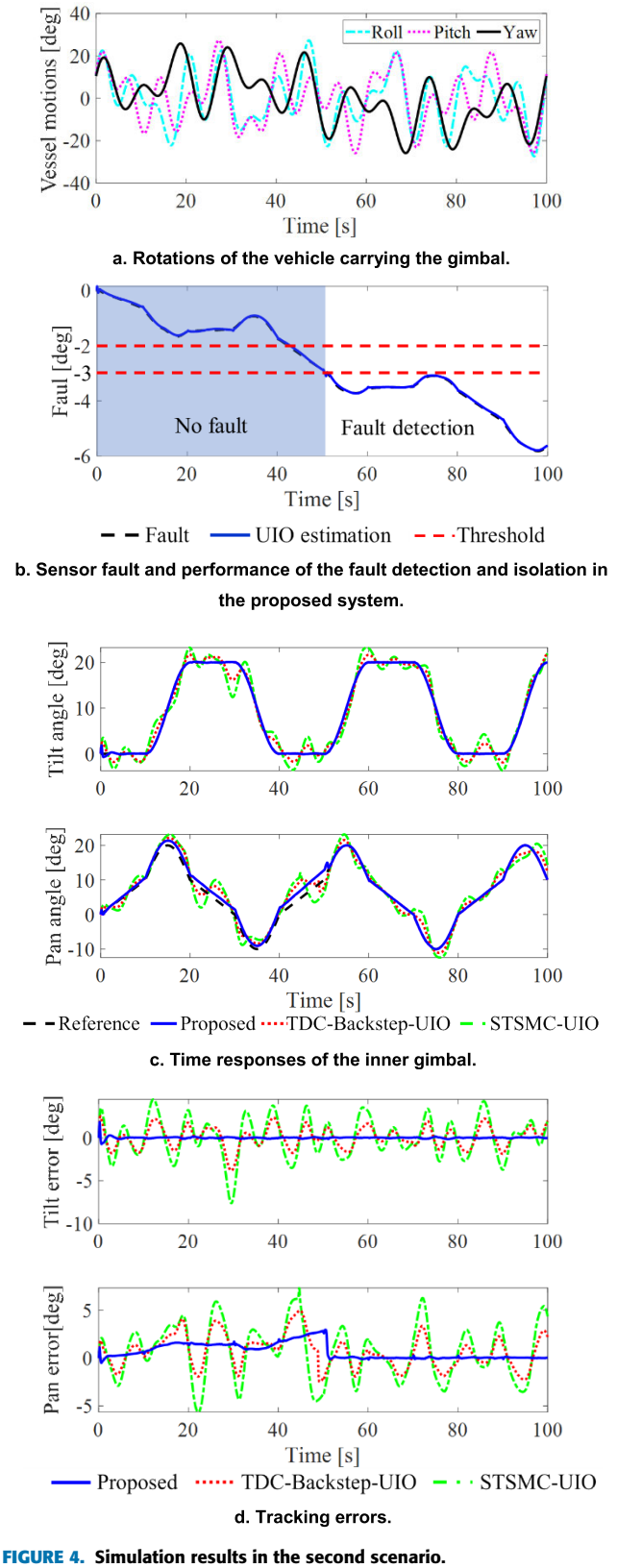

FIGURE 4. Simulation results in the second scenario.

integral control law. The results, shown in Fig. 4c and 4d, imply that the faults were compensated. Comparing the tracking errors to the amplitude of the vessel motions, both

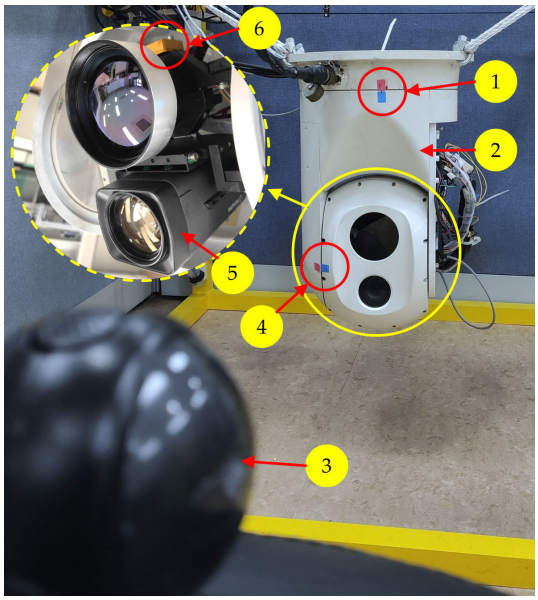

FIGURE 5. The apparatus setup for validation. (1) Position markers; (2) 2-axis gimbal; (3) External camera; (4) Position markers; (5) Vision camera; (6) AHRS.

STSMC and TDC-Backstep has significantly suppressed the disturbances. However, due to input delay, the disturbance rejections were not excellent, and large oscillations were still available in the responses. The proposed control law, on the other hand, provided effective performances in both tracking and disturbance rejection. These results came from the proper estimation of the disturbances presented in section III.C.

B. EXPERIMENTAL STUDIES

Two experiments were conducted, one was with the normal operating condition of the apparatus, and the other was affected by purposive input disturbances to replicate the worst-case scenario. The configuration of the experimental apparatus is shown in Fig. 5. The real fault of the sensor was estimated by the UIO, as in Fig. 6a and 8b. However, it was difficult to determine the actual rotation of the system itself and, therefore, to confirm the fault estimation. Instead, by considering the motion of the projection of a static point on the image plane of the camera, which is the tracking device mounted on the inner gimbal, the control performance could be deduced. The idea is that in the periodic rotations of the inner gimbal, the relative position of the camera's LOS and a fixed point in the reference coordinate repeats with each period. The image tracker from [41] was used, and the responses of the image coordinates were recorded. From the pinhole camera model, the measurements from the image tracker relate to the rotation of the inner gimbal as follows.

$$\begin{bmatrix} \dot{x} \\ \dot{y} \end{bmatrix} = \frac{1}{Z_c} \begin{bmatrix} x & f & 0 \\ y & 0 & f \end{bmatrix} \begin{bmatrix} \omega_{tx} \\ \omega_{ty} \\ \omega_{tz} \end{bmatrix} \tag{45}$$

$[\, x \;\; y \,]^T$ is the location of the projection on the image plane. f is the camera focal length and Z_c is the distance to the

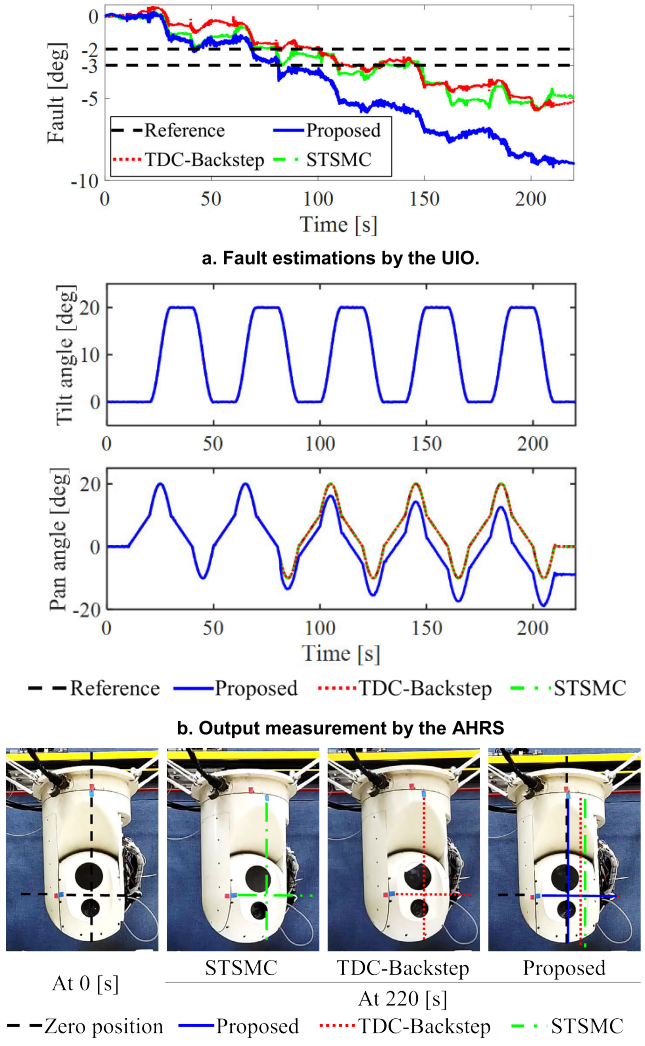

a. Fault estimations by the UIO.

b. Output measurement by the AHRS

c. Positions of the system at the beginning and the end of the experiment.

FIGURE 6. Tracking performance in the first experiment.

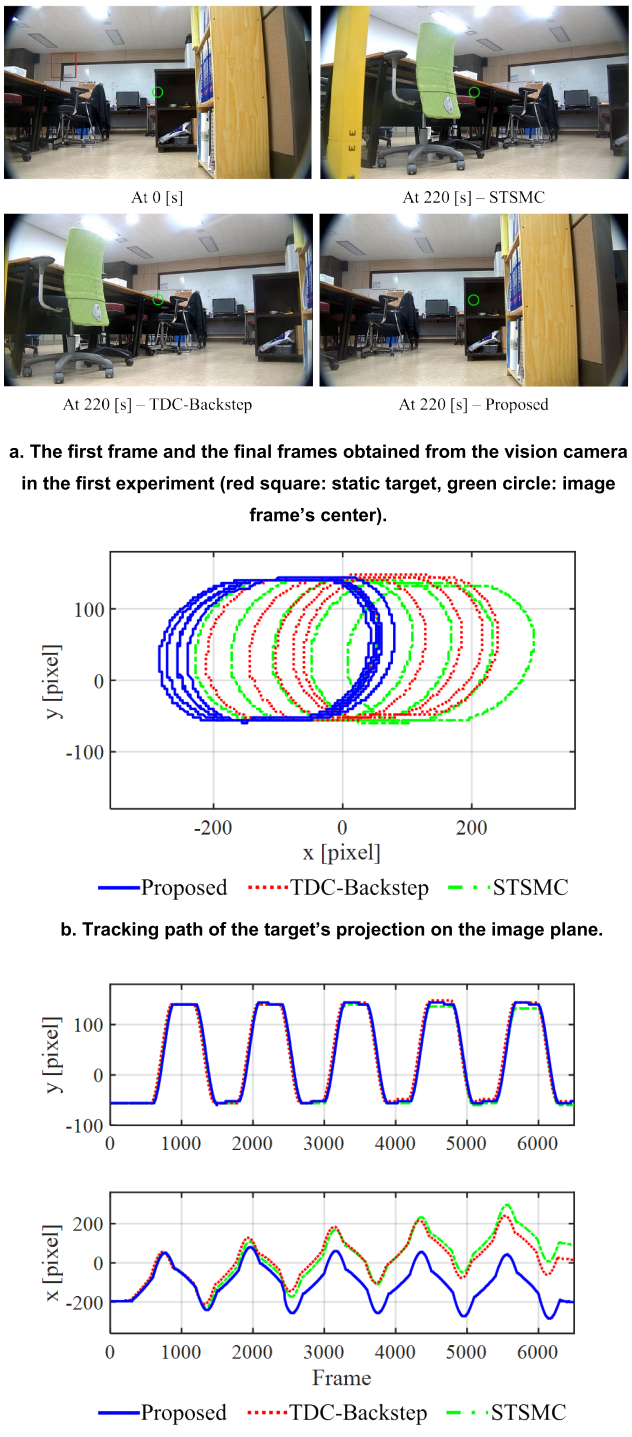

a. The first frame and the final frames obtained from the vision camera in the first experiment (red square: static target, green circle: image frame's center).

b. Tracking path of the target's projection on the image plane.

c. Time response of each image coordinate.

FIGURE 7. Location of the target's projection on the image plane during the first experiment.

target; both are constants. Hence, the projection draws the same trajectory on the image plane in every period, if the inner gimbal repeats its periodic rotations. These results are given in Fig. 7, 8c, and 8d, and compared to the AHRS's measurements.

The tracking performances in the first experiment are drawn in Fig. 6 and 7. The results show that the STSMC and the TDC-Backstep controllers regulated the system such that the measured outputs properly followed the desired trajectories. The AHRS indicated that the tilt and pan rotations at the beginning and the end of the experiments are both 0 [deg]. However, as seen in Fig. 6c, the actual positions of the gimbal at the end of the experiment were different from those at the beginning. The gimbal remained positive pan angles at the end, though the measured values were zeros; thus, the presence of the sensor fault is confirmed. In the same manner, the corresponding trajectories of the projection initial at the corner tended to the right and slightly upward on the image plane, as in Fig. 7. While the upward trend was actually the result of the camera's imaging geometry [41], the horizontal drift of the projection revealed the AHRS yaw drift. Thus, the measured pan rotation was smaller than the true value, so the outer channel performed a greater rotation than it should truly be.

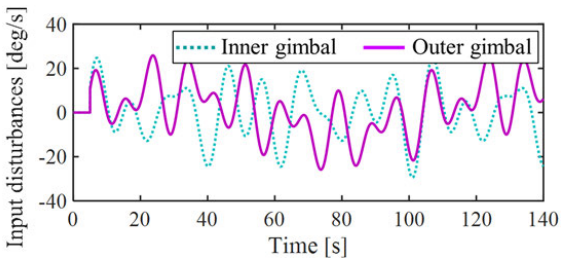

a. Input disturbances.

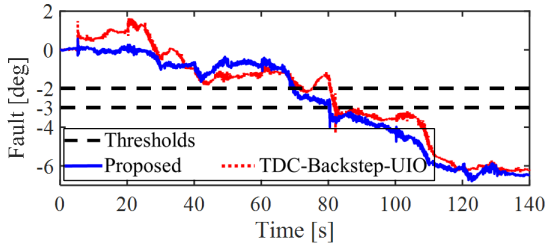

b. Fault estimations.

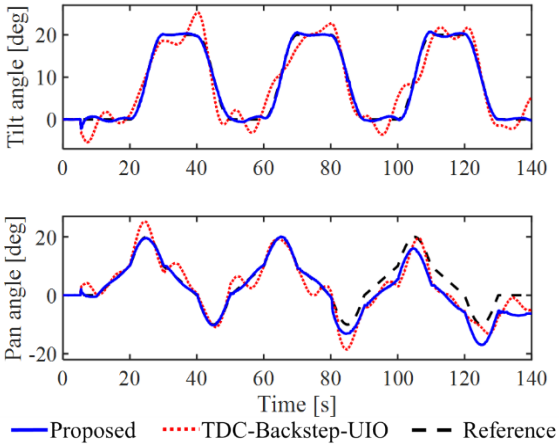

c. Output measurement by the AHRS.

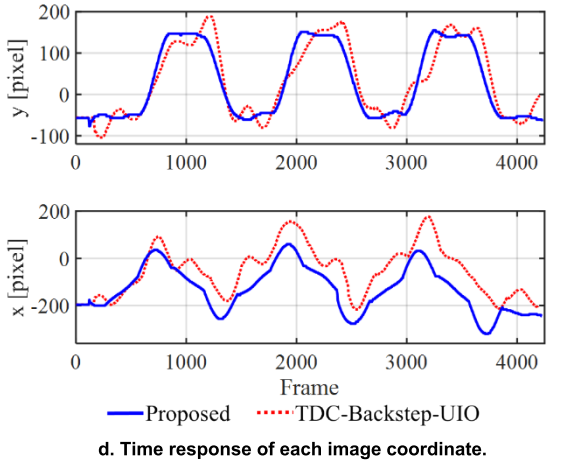

d. Time response of each image coordinate.

FIGURE 8. Tracking performance in the second experiment.

The estimations by the UIO also showed a similar trend of the sensor fault. In the system controlled by the proposed controller, the estimated value began to be greater than the upper threshold from 70 [s], thus the fault was confirmed. Subsequently, the response of the pan rotation operated by the proposed fault-tolerant controller diverted from the sensor measurement and followed the feedback from the UIO's estimation of the pan angle. The results obtained by the image tracker show that the response returned to its true desired value, and thus, the tracking path did not drift away. Therefore, the efficiency of the proposed system was validated.

The experimental results conducted in the second scenario are given in Fig. 8. The combination of the TDC-Backstep controller and the UIO was compared to the proposed control system. For a fair comparison, the input disturbances shown in Fig. 8a were added to both systems. Fig. 8b shows the estimations of the fault while the tracking routes are deduced from Fig. 8c and 8d. As shown in these figures, the proposed control system achieved much better performance in both gimbal channels. Even though, the disturbances still resulted in small oscillations on the tracking route, due to the delayed input. For the tilt rotation, the root-mean-square error reduced up to 84.38% compared to that of the TDC-Backstep control. For the pan rotation, the fault alarms were set at 80 [s] and 82 [s] in the respective tests with the proposed controller and the comparative one. The fault-tolerant performances were validated as the projections returned to their initial locations at the end of the experiments.

VI. CONCLUSION

This paper has solved the problem of fault isolation and fault-tolerant control of the gimbal system affected by time-varying delay and disturbances. The unpredicted fault occurred at the yaw measurement of the AHRS, which is well known as the yaw drift phenomenon. The characteristic of the fault was unknown, but the model of the faulty system was able to be derived in this paper. Then, the fault-tolerant controller was designed to ensure the tracking performance to be tolerant to the fault and robust to the time delay and disturbances. The fault and disturbances were estimated based on the concept of the UIO and LMI. And the robust control law was designed based on the backstepping technique and the integral sliding mode with the super-twisting algorithm.

Simulations and experiments were performed. Their results validated the efficiency of the proposed control system. Compared to the controller designed in the previous study, the superiorities of the proposed control scheme can be summarized in two aspects:

- Fault-tolerant performances: The proposed FTC properly estimated and effectively compensated for the sensor fault. Thus, reliable tracking results were obtained without the need for additional measurement devices.

- Robust performances: The combination of the disturbance estimation of the UIO and the robust integral sliding mode control technique resulted in effective disturbance rejection. Thus, the proposed FTC was able to maintain adequate performance in the presence of disturbances.

Unfortunately, even the most advanced control law still cannot surpass the primary limitation of low-spec hardware, such as the delay. For better performance, there is a need

for real-time control systems. In that case, the imaging measurement can be used, for example through a Kalman filter, to correct the measurement of the sensor.

APPENDIX A

With the dynamics of the estimation error's given in Equation (15), the time derivative of the Lyapunov function candidate V_{UIO} is derived as:

$$\begin{aligned}\dot{V}_{UIO} &= \tilde{\boldsymbol{X}}^{\boldsymbol{T}}\boldsymbol{P}\dot{\tilde{\boldsymbol{X}}} + \dot{\tilde{\boldsymbol{X}}}^{\boldsymbol{T}}\boldsymbol{P}\tilde{\boldsymbol{X}} \\ &= -\tilde{\boldsymbol{X}}^{T}\left(\boldsymbol{C}_{\boldsymbol{X}}^{T}\boldsymbol{H}^{T}\boldsymbol{P} + \boldsymbol{P}\boldsymbol{H}\boldsymbol{C}_{\boldsymbol{X}}\right)\tilde{\boldsymbol{X}} \\ &\quad + 2\tilde{\boldsymbol{X}}^{T}\boldsymbol{P}\boldsymbol{E}\left(\boldsymbol{F}\left(\boldsymbol{X}\right)\boldsymbol{X} - \boldsymbol{F}\left(\hat{\boldsymbol{X}}\right)\hat{\boldsymbol{X}}\right) \\ &\quad + 2\tilde{\boldsymbol{X}}^{T}\boldsymbol{P}\boldsymbol{E}\boldsymbol{B}_{\boldsymbol{X}}\left(\boldsymbol{u}_{\boldsymbol{\tau}} - \bar{\boldsymbol{u}}_{\boldsymbol{\tau}}\right)\end{aligned} \tag{A.1}$$

Applying Young's inequality and the inequality given in Eq. (8) for the second term of $\dot{V}_{UIO}$ yields that:

$$\begin{aligned}&2\tilde{\boldsymbol{X}}^{T}\boldsymbol{P}\boldsymbol{E}\left(\boldsymbol{F}\left(\boldsymbol{X}\right)\boldsymbol{X} - \boldsymbol{F}\left(\hat{\boldsymbol{X}}\right)\hat{\boldsymbol{X}}\right) \\ &\quad\leq \tilde{\boldsymbol{X}}^{T}\boldsymbol{E}^{T}\boldsymbol{P}\boldsymbol{P}\boldsymbol{E}\tilde{\boldsymbol{X}} \\ &\qquad + \left(\boldsymbol{F}\left(\boldsymbol{X}\right)\boldsymbol{X} - \boldsymbol{F}\left(\hat{\boldsymbol{X}}\right)\hat{\boldsymbol{X}}\right)^{T}\left(\boldsymbol{F}\left(\boldsymbol{X}\right)\boldsymbol{X} - \boldsymbol{F}\left(\hat{\boldsymbol{X}}\right)\hat{\boldsymbol{X}}\right) \\ &\quad\leq \tilde{\boldsymbol{X}}^{T}\left(\boldsymbol{E}^{T}\boldsymbol{P}\boldsymbol{P}\boldsymbol{E} + \kappa\boldsymbol{I}\right)\tilde{\boldsymbol{X}}\end{aligned} \tag{A.2}$$

Similarly, the third term of $\dot{V}_{UIO}$ follows the Youngs's inequality resulting:

$$\begin{aligned}2\tilde{\boldsymbol{X}}^{T}\boldsymbol{P}\boldsymbol{E}\boldsymbol{B}_{\boldsymbol{X}}\left(\boldsymbol{u}_{\boldsymbol{\tau}} - \bar{\boldsymbol{u}}_{\boldsymbol{\tau}}\right) \leq \frac{1}{\gamma^{2}}\tilde{\boldsymbol{X}}^{T}\bar{\boldsymbol{B}}_{\boldsymbol{X}}^{T}\boldsymbol{E}^{T}\boldsymbol{P}\boldsymbol{P}\boldsymbol{E}\bar{\boldsymbol{B}}_{\boldsymbol{X}}\tilde{\boldsymbol{X}} \\ + \gamma^{2}\left(\boldsymbol{u}_{\boldsymbol{\tau}} - \bar{\boldsymbol{u}}_{\boldsymbol{\tau}}\right)^{T}\boldsymbol{B}_{\boldsymbol{X}}^{T}\boldsymbol{B}_{\boldsymbol{X}}\left(\boldsymbol{u}_{\boldsymbol{\tau}} - \bar{\boldsymbol{u}}_{\boldsymbol{\tau}}\right)\end{aligned} \tag{A.3}$$

Substituting the inequalities into Eq. (A.1) results in:

$$\begin{aligned}\dot{V}_{UIO} \leq \tilde{\boldsymbol{X}}^{T}\Big(&-\boldsymbol{C}_{\boldsymbol{X}}^{T}\boldsymbol{H}^{T}\boldsymbol{P} - \boldsymbol{P}\boldsymbol{H}\boldsymbol{C}_{\boldsymbol{X}} + \boldsymbol{E}^{T}\boldsymbol{P}\boldsymbol{P}\boldsymbol{E} + \kappa\boldsymbol{I} \\ &+ \frac{1}{\gamma^{2}}\bar{\boldsymbol{B}}_{\boldsymbol{X}}^{T}\boldsymbol{E}^{T}\boldsymbol{P}\boldsymbol{P}\boldsymbol{E}\bar{\boldsymbol{B}}_{\boldsymbol{X}}\Big)\tilde{\boldsymbol{X}} \\ &+ \gamma^{2}\left(\boldsymbol{u}_{\boldsymbol{\tau}} - \bar{\boldsymbol{u}}_{\boldsymbol{\tau}}\right)^{T}\boldsymbol{B}_{\boldsymbol{X}}^{T}\boldsymbol{B}_{\boldsymbol{X}}\left(\boldsymbol{u}_{\boldsymbol{\tau}} - \bar{\boldsymbol{u}}_{\boldsymbol{\tau}}\right)\end{aligned} \tag{A.4}$$

APPENDIX B

Let each element of the vector $\boldsymbol{\varepsilon} = [\,\varepsilon_1\ \varepsilon_1\,]^T$ be expressed as $\varepsilon_i = \varepsilon_{1i} + \int_0^t \varepsilon_{2i}\left(\tau\right)d\tau$ denoting that in general, the remaining term ε_i can be considered as matched disturbances ε_{2i} and unmatched disturbance ε_{1i}. Assume that the unmatched disturbances can be expressed as $\varepsilon_{1i} = \eta_i\sqrt{|s_i|}$, and disturbances are bounded by non-negative constants $|\eta_i| \leq E_{1i}$ and $|\varepsilon_{2i}| \leq E_{2i}$. With the signum-like function in Eq. (43), the modified sliding manifold of each gimbal channel can be rewritten as follows:

$$\begin{aligned}\dot{s}_i &= -g_{1i}\sqrt{|s_i|}\text{sign}\left(s_i\right) + x_i + \upsilon_{1i} \\ \dot{x}_i &= -g_{2i}\text{sign}\left(s_i\right) + \upsilon_{2i}\end{aligned} \tag{B.1}$$

where:

$$\begin{aligned}\upsilon_{1i} &= \eta_i\sqrt{|s_i|} + g_{1i}\sqrt{|s_i|}\text{sign}\left(s_i\right)\frac{\delta_i}{|s_i| + \delta_i} \\ &= \left(\eta_i + g_{1i}\text{sign}\left(s_i\right)\frac{\delta_i}{|s_i| + \delta_i}\right)\sqrt{|s_i|} \\ &= \mu_i\sqrt{|s_i|} \\ \upsilon_{2i} &= \varepsilon_{2i} + g_{2i}\text{sign}\left(s_i\right)\frac{\delta_i}{|s_i| + \delta_i}\end{aligned} \tag{B.2}$$

Seeber and Horn [36] declared that the essential conditions of the controller gains, such that the system presented by Eq. (B.1) is finite-time stable, are given by:

$$\begin{aligned}g_{2i} &> \max|\upsilon_{2i}| \\ g_{1i} &> \max|\mu_i| + \sqrt{g_{2i} + \max|\upsilon_{2i}|}\end{aligned} \tag{B.3}$$

In other words, they are:

$$\begin{aligned}g_{2i} &> E_{2i} + g_{2i}\frac{\delta_i}{|s_i| + \delta_i} \\ g_{1i} &> E_{1i} + g_{1i}\frac{\delta_i}{|s_i| + \delta_i} + \sqrt{g_{2i} + E_{2i} + g_{2i}\frac{\delta_i}{|s_i| + \delta_i}}\end{aligned} \tag{B.4}$$

The inequalities in Eq. (B.4) are respectively equivalent to the following restriction of the sliding variable s_i:

$$\begin{aligned}|s_i| &> \frac{\delta_i}{g_{2i} - E_{2i}} \\ |s_i| &> \frac{\delta_i\left(2E_{1i}g_{1i} + g_{2i}\right) + \sqrt{g_{2i}^2 + 2E_{1i}g_{1i}g_{2i} + 4g_{1i}^2E_{2i}}}{2g_{1i}^2 - \left(2E_{1i}g_{1i} + g_{2i}\right) + \sqrt{g_{2i}^2 + 2E_{1i}g_{1i}g_{2i} + 4g_{1i}^2E_{2i}}}\end{aligned} \tag{B.5}$$

In summary, the sliding variable s_i always converges to the compact set defined by:

$$\begin{aligned}s_i \leq \max\Bigg(&\frac{\delta_i}{g_{2i} - E_{2i}}, \\ &\frac{\delta_i\left[\left(2E_{1i}g_{1i} + g_{2i}\right) + \sqrt{g_{2i}^2 + 2E_{1i}g_{1i}g_{2i} + 4g_{1i}^2E_{2i}}\right]}{2g_{1i}^2 - \left(2E_{1i}g_{1i} + g_{2i}\right) + \sqrt{g_{2i}^2 + 2E_{1i}g_{1i}g_{2i} + 4g_{1i}^2E_{2i}}}\Bigg)\end{aligned} \tag{B.6}$$

This implies the ultimate boundedness of the control system. The size of the set depends on the values of the controller's gains and the supremum norm of disturbances. The higher the controller's gains are, the smaller the size of the set.

REFERENCES

[1] C. E. Lin and S.-K. Yang, "Camera gimbal tracking from UAV flight control," in *Proc. Int. Autom. Control Conf. (CACS)*, Nov. 2014, pp. 319–322.
[2] S.-N. Lim, A. Elgammal, and L. S. Davis, "Image-based pan-tilt camera control in a multi-camera surveillance environment," in *Proc. Int. Conf. Multimedia Expo.*, 2003, vol. 1, no. 3, p. 645.
[3] X. Liu, J. Mao, J. Yang, S. Li, and K. Yang, "Robust predictive visual servoing control for an inertially stabilized platform with uncertain kinematics," *ISA Trans.*, vol. 114, pp. 347–358, Aug. 2021.
[4] Z. Hurak and M. Rezac, "Image-based pointing and tracking for inertially stabilized airborne camera platform," *IEEE Trans. Control Syst. Technol.*, vol. 20, no. 5, pp. 1146–1159, Sep. 2012.
[5] J. M. Hilkert, "Inertially stabilized platform technology concepts and principles," *IEEE Control Syst. Mag.*, vol. 28, no. 1, pp. 26–46, Feb. 2008.

[6] M. K. Masten, "Inertially stabilized platforms for optical imaging systems," *IEEE Control Syst.*, vol. 28, no. 1, pp. 47–64, Feb. 2008.
[7] P. J. Kennedy and R. L. Kennedy, "Direct versus indirect line of sight (LOS) stabilization," *IEEE Trans. Control Syst. Technol.*, vol. 11, no. 1, pp. 3–15, Jan. 2003.
[8] M. Abdo, A. R. Vali, A. Toloei, and M. R. Arvan, "Research on the cross-coupling of a two axes gimbal system with dynamic unbalance," *Int. J. Adv. Robot. Syst.*, vol. 10, no. 10, p. 357, Oct. 2013.
[9] J. M. Osborne and R. Fuentes, "Global analysis of the double-gimbal mechanism," *IEEE Control Syst.*, vol. 28, no. 4, pp. 44–64, Aug. 2008.
[10] D. H. Lee, D. Q. Tran, Y. B. Kim, and S. Chakir, "A robust double active control system design for disturbance suppression of a two-axis gimbal system," *Electronics*, vol. 9, no. 10, pp. 1–18, 2020.
[11] O. A. Sushchenko and A. A. Tunik, "Robust optimization of the inertially stabilized platforms," in *Proc. 2nd Int. Conf. Methods Syst. Navigat. Motion Control (MSNMC)*, Oct. 2012, pp. 101–105.
[12] Z. Ding, F. Zhao, Y. Lang, Z. Jiang, and J. Zhu, "Anti-disturbance neural-sliding mode control for inertially stabilized platform with actuator saturation," *IEEE Access*, vol. 7, pp. 92220–92231, 2019.
[13] M. F. Reis, J. C. Monteiro, R. R. Costa, and A. C. Leite, "Super-twisting control with quaternion feedback for a 3-DoF inertial stabilization platform," in *Proc. IEEE Conf. Decis. Control (CDC)*, Dec. 2018, pp. 2193–2198.
[14] J. Mao, J. Yang, X. Liu, S. Li, and Q. Li, "Modeling and robust continuous TSM control for an inertially stabilized platform with couplings," *IEEE Trans. Control Syst. Technol.*, vol. 28, no. 6, pp. 2548–2555, Nov. 2020.
[15] H. Li and J. Yu, "Anti-disturbance control based on cascade ESO and sliding mode control for gimbal system of double gimbal CMG," *IEEE Access*, vol. 8, pp. 5644–5654, 2020.
[16] Z. Diao, H. Quan, L. Lan, and Y. Han, "Analysis and compensation of MEMS gyroscope drift," in *Proc. 7th Int. Conf. Sens. Technol. (ICST)*, Dec. 2013, pp. 592–596.
[17] J. Georgy, A. Noureldin, M. J. Korenberg, and M. M. Bayoumi, "Modeling the stochastic drift of a MEMS-based gyroscope in gyro/odometer/GPS integrated navigation," *IEEE Trans. Intell. Transp. Syst.*, vol. 11, no. 4, pp. 856–872, Dec. 2010.
[18] S. Li, Y. Gao, G. Meng, G. Wang, and L. Guan, "Accelerometer-based gyroscope drift compensation approach in a dual-axial stabilization platform," *Electronics*, vol. 8, no. 5, p. 594, May 2019.
[19] D. Giansanti, G. Maccioni, and V. Macellari, "Guidlines for calibration and drift compensation of a wearable device with rate-gyroscopes and accelerometers," in *Proc. 29th Annu. Int. Conf. Eng. Med. Biol. Soc.*, Aug. 2007, pp. 2342–2345.
[20] I. Hwang, S. Kim, Y. Kim, and C. E. Seah, "A survey of fault detection, isolation, and reconfiguration methods," *IEEE Trans. Control Syst. Technol.*, vol. 18, no. 3, pp. 636–653, May 2010.
[21] M. Blanke, M. Staroswiecki, and N. E. Wu, "Concepts and methods in fault-tolerant control," in *Proc. Amer. Control Conf.*, vol. 4, Jun. 2001, pp. 2606–2620.
[22] A. Abbaspour, S. Mokhtari, A. Sargolzaei, and K. K. Yen, "A survey on active fault-tolerant control systems," *Electronics*, vol. 9, no. 9, p. 1513, Sep. 2020.
[23] H. Nour, D. Theilliol, J.-C. Ponsart, and A. Chamseddine, *Fault-Tolerant Control Systems*. London, U.K.: Springer, 2009.
[24] H. V. Dao, D. T. Tran, and K. K. Ahn, "Active fault tolerant control system design for hydraulic manipulator with internal leakage faults based on disturbance observer and online adaptive identification," *IEEE Access*, vol. 9, pp. 23850–23862, 2021.
[25] H. V. A. Truong, H. A. Trinh, D. T. Tran, and K. K. Ahn, "A robust observer for sensor faults estimation on n-DOF manipulator in constrained framework environment," *IEEE Access*, vol. 9, pp. 88439–88451, 2021.
[26] V. D. Phan, C. P. Vo, H. V. Dao, and K. K. Ahn, "Robust fault-tolerant control of an electro-hydraulic actuator with a novel nonlinear unknown input observer," *IEEE Access*, vol. 9, pp. 30750–30760, 2021.
[27] V.-P. Vu, V.-T. Ngo, V.-D. Do, D.-N. Truong, N. V. Quynh, P. D.-H. Bui, V. T. Mai, and T. D. Do, "Polynomial observer-based controller synthesis and fault-tolerant control for tracking optimal power of wind energy conversion systems," *IEEE Access*, vol. 8, pp. 150130–150141, 2020.
[28] V. D. Phan, C. P. Vo, H. V. Dao, and K. K. Ahn, "Actuator fault-tolerant control for an electro-hydraulic actuator using time delay estimation and feedback linearization," *IEEE Access*, vol. 9, pp. 107111–107123, 2021.
[29] K. Xiahou, Y. Liu, L. Wang, M. S. Li, and Q. H. Wu, "Switching fault-tolerant control for DFIG-based wind turbines with rotor and stator current sensor faults," *IEEE Access*, vol. 7, pp. 103390–103403, 2019.
[30] J. Baillieul and P. J. Antsaklis, "Control and communication challenges in networked real-time systems," *Proc. IEEE*, vol. 95, no. 1, pp. 9–28, Jan. 2007.
[31] J.-P. Richard, "Time-delay systems: An overview of some recent advances and open problems," *Automatica*, vol. 39, no. 10, pp. 1667–1694, 2003.
[32] T. Huynh, M.-T. Tran, D.-H. Lee, and Y.-B. Kim, "A study on robust fault-tolerant control for a low-cost target tracking system," in *Proc. 21st Int. Conf. Control, Automat. Syst. (ICCAS)*, 2021.
[33] H.-C. Park, S. Chakir, Y.-B. Kim, and T. Huynh, "A nonlinear backstepping controller design for high-precision tracking applications with input-delay gimbal systems," *J. Mar. Sci. Eng.*, vol. 9, no. 5, p. 530, May 2021.
[34] S. Boyd, L. El Ghaoui, E. Feron, and V. Balakrishnan, *Linear Matrix Inequalities in System and Control Theory*. Philadelphia, PA, USA: Society for Industrial and Applied Mathematics, 1994.
[35] L. Fridman, J. Moreno, and R. Iriarte, *Sliding Modes after the First Decade of the 21st Century*, vol. 412. Berlin, Germany: Springer, 2012.
[36] R. Seeber and M. Horn, "Stability proof for a well-established super-twisting parameter setting," *Automatica*, vol. 84, pp. 241–243, Oct. 2017.
[37] J. A. Moreno and M. Osorio, "Strict Lyapunov functions for the super-twisting algorithm," *IEEE Trans. Autom. Control*, vol. 57, no. 4, pp. 1035–1040, Apr. 2012.
[38] A. Levant, "Principles of 2-sliding mode design," *Automatica*, vol. 43, no. 4, pp. 576–586, 2007.
[39] S. Seshagiri and H. K. Khalil, "On introducing integral action in sliding mode control," in *Proc. 41st IEEE Conf. Decis. Control*, Dec. 2002, pp. 1473–1478.
[40] L. Peng, M. Jian-jun, L. Wen-qiang, and Z. Zhi-qiang, "Adaptive conditional integral sliding mode control for fault tolerant flight control system," in *Proc. 7th Int. Conf. Syst. Simul. Sci. Comput.*, Oct. 2008, pp. 638–642.
[41] T. Huynh, M.-T. Tran, D.-H. Lee, S. Chakir, and Y.-B. Kim, "A study on vision-based backstepping control for a target tracking system," *Actuators*, vol. 10, no. 5, p. 105, May 2021.

THINH HUYNH received the Bachelor of Engineering and Master of Engineering degrees in vehicle engineering from Ho Chi Minh City University of Technology and Education (HCMUTE), Vietnam, in 2014 and 2016, respectively. He is currently pursuing the Ph.D. degree with the Department of Smart Robot Convergence and Application Engineering, Pukyong National University, Busan, South Korea, under the supervision of Prof. Young-Bok Kim. Since 2017, he has been with the Department of Chassis and Body, HCMUTE, Vietnam. His research interests include control engineering, robotics, and automotive engineering.

YOUNG-BOK KIM (Senior Member, IEEE) received the B.S. and M.S. degrees in mechanical system engineering from Pukyong National University, Busan, South Korea, and the Ph.D. degree from Kobe University, Kobe, Japan, in 1996. He has held a visiting position at the Department of Mechanical Engineering, University of Maryland, College Park, MD, from 2011 to 2012. He is currently a Professor with the Department of Smart Robot Convergence and Application Engineering, Pukyong National University. His research interests include control theory and application with dynamic ship positioning and autonomous control system design. He is a member of ICASE, KSME, and ASME.